http://dx.doi.org/10.1097/mm9.0000000000000008

MedMat

Original Research

OPEN

Adaptive dual-responsive nanocapsules for precision ferroptosis-driven and chemotherapy-enhanced tumor ablation

Jia You[a], Shikang Liu[a], Jiarong Liang[a], Qiaoli Feng[b], Mengdie Duan[a], Zeeshan Ali[c], Lujia Chen[b], Zhiyi Wang[d,*]

Abstract

Tumors increasingly threaten human health, with rising incidence and mortality rates. Treatment complexity, including individual differences and tumor molecular characteristics, limits clinical application potential. Ferroptosis, a new strategy for tumor treatment, has stirred much interest. However, the dense properties and unique physiological environment of tumor tissues limit the ability of ferroptosis agents to work inside tumors. In this study, intelligent temperature and pH dual-responsive nanocapsules were designed for tumor therapy. The nanocapsules leverage the unique physiological environment of tumors, where both acidity and temperature can be exploited to trigger drug release. The core materials of the nanocapsules are a polylactic acid-glycolic acid copolymer and poly(N-isopropyl acrylamide), which ensure biocompatibility and responsiveness to the tumor microenvironment. These nanocapsules encapsulate amorphous iron nanoparticles as ferroptosis agents and tirapazamine as a chemotherapeutic drug, enabling a combination therapy approach. Once introduced into the tumor, the nanocapsules change size in response to the local acidic and thermal conditions, releasing their payload. This targeted approach enhances drug delivery efficiency, reduces toxicity to surrounding healthy tissues, and promotes ferroptosis in tumor cells. The study demonstrated the nanocapsules' ability to inhibit tumor growth both in vitro and in vivo while maintaining excellent biocompatibility and biosafety, making it a promising candidate for advanced cancer therapies.

Keywords: Combination therapy, Ferroptosis, Nanodrug delivery system, Tumor therapy

1. Introduction

Recently, tumors, as a chronic disease, have gradually threatened the health of human beings, and their prevalence and mortality rates have shown a trend of increasing annually. Multiple factors such as lifestyle, hereditary factors, and environmental exposures are responsible for the high morbidity and mortality of tumor diseases.[1] Despite improvements in early screening and prevention, morbidity and mortality from tumor patients continue to rise yearly, not only underscoring the high risk of oncologic disease but also triggering an urgent demand for more effective treatment means. Currently, the primary treatments for patients with tumors include surgical resection, radiation therapy, chemotherapy, endocrine therapy, immunotherapy, etc.[2–5] Although these treatments have improved the survival rate of tumor patients to a certain extent, some still face unanticipated problems in practical application, such as the emergence of drug resistance from long-term drug therapy, the absence of targets of tumor cells, and the side effects caused by drug therapy.[6,7] These less common but notable challenges urgently require new solutions to advance treatment outcomes.

In recent years, ferroptosis has been recognized as an influential strategy for tumor therapy.[8] Ferroptosis, as a unique form of regulated cell death, was first proposed by Dixon et al[9] and characterized by excessive accumulation of intracellular reactive oxygen species (ROS) and lipid peroxidation (LPO).[10] The cell death mechanism is regulated by a variety of signals, including ROS, glutathione peroxidase (GPX4), and heat shock proteins. The core mechanism is that excess iron and intracellular hydrogen peroxide (H_2O_2) promote the Fenton reaction ($Fe^{2+} + H_2O_2 \rightarrow Fe^{3+} + OH^- + \cdot OH$), increasing the levels of LPO and hydroxyl radicals (·OH).[11,12] Its intrinsic pharmacological features are capable of modulating the proliferation of tumor cells. However, the dense properties and unique physiological environment of tumor tissues ferroptosis limit the penetration and effectiveness of ferroptosis-inducing agents. Fortunately, nano-delivery systems make it possible for ferroptosis-mediated tumor therapy. Due to the unique physicochemical properties of nanocomposite, it is not only able to introduce new properties such as photothermal properties and magnetic properties but also to effectively deliver ferroptosis agents to the deeper regions of the tumor.[13,14]

[a]Spin-X Institute, School of Chemistry and Chemical Engineering, State Key Laboratory of Luminescent Materials and Devices, South China University of Technology, Guangzhou, China, [b]Breast Center, Department of General Surgery, Nanfang Hospital, Southern Medical University, Guangzhou, China, [c]School of Chemical and Materials Engineering (SCME), National University of Sciences and Technology, Islamabad, Pakistan, [d]School of Materials, Sun Yat-Sen University, Shenzhen, China.

**Corresponding author: Address: Zhiyi Wang, Spin Technology Research Institute, School of Materials, Sun Yat-Sen University, Guangzhou International Campus, South China University of Technology, Guangzhou, Guangdong Province, China. E-mail address: wangzhiyi2020@scut.edu.cn (Z. Wang).*

Jia You and Shikang Liu contributed equally to this work

Supplemental Digital Content is available for this article.

MedMat (2025) 1:2

Received: 15 September 2024; Accepted 27 September 2024

Published online xxx xx 2024

In this study, we engineered novel multifunctional nanocapsules that respond to changes in temperature and pH, allowing for controlled drug release. It comprises polylactic acid-glycolic acid copolymer (PLGA) and poly(*N*-isopropyl acrylamide) (PNIPAM) as vehicles for drug delivery. PLGA is characterized by its biocompatibility, degradability, and size adjustability, which enables the precise release of the drug in the faintly acidic tumor microenvironment. Temperature-responsive PNIPAM was grafted to its surface to promote drug release through the photothermal effect, thus realizing the deep delivery of ferroptosis agents (Figure 1). The nanocapsules were prepared by microemulsion method[15,16] utilizing PLGA-PNIPAM as the backbone, combined with amorphous iron (AFe) nanoparticles with Fenton-responsive activity, photothermal agent Y6, and chemotherapeutic agent tirapazamine (TPZ). The multifunctional nanocarrier is designed to provide an integrated tumor treatment regimen through ferroptosis, photothermal therapy, and chemotherapy. By virtue of the appropriate size of the nanocarriers, they can be efficiently enriched at the tumor loci. Based on the acid sensitivity of PLGA and the temperature sensitivity of PNIPAM and Y6 molecules in the nanocapsules, they can realize responsive degradation under the dual stimulation of the faintly acidic tumor microenvironment and photothermal effect, facilitating the release of small internal payloads for therapeutic effects in the oxygen-poor deep tumor tissues.[17–20] The nanocapsules enable the delivery of drugs to the cancer cells as efficiently and quickly as possible to exert anticancer effects, while the promising biocompatibility proved its potential for practical applications.

2. Experimental section

2.1 Materials and reagents

Tirapazamine and oleylamine were purchased from Macklin Chemicals. Y6 was purchased from J&W Technology. Dimethyl sulfoxide (DMSO) methylene chloride and *n*-hexane were purchased from Sarn Chemical Technology (Shanghai). Pentacarbonyl iron ($Fe(CO)_5$) was purchased from Jiangsu Tianyi. 1-Octadeene was purchased from Sigma-Aldrich. Pancreatin and phosphate buffer were purchased from Thermo Fisher Scientific. The CCK-8 kit, 2′,7′-dichlorofluorescein diacetate (DCFH-DA), and annexin V-FITC/PI apoptosis detection kit were purchased from Beyotime Biotechnology. All the chemicals were used without additional purification, except DMSO, $CHCl_3$, triethylamine, and *n*-hexane. Deionized (DI) water was obtained from a Milli-Q water purification system.

2.2 Characterization

The morphology of prepared nanoparticles was observed by transmission electron microscopy (TEM, JEM 2100, Japan). X-ray diffractions (XRDs) of samples were recorded on a D/max-2550 PC X-ray diffractometer (Rigaku, Japan). UV–vis–near-infrared (NIR) absorption spectra were measured on a Shimadz spectrophotometer (UV-3150, Japan). Fourier transform infrared spectra were recorded using a Shimadz spectrophotometer (IRTracer-100, Japan). Size distribution and Zeta potential of the samples were recorded using the Zetasizer Nano ZS apparatus (Malvern, UK). The generation of free radicals was characterized by electron paramagnetic resonance spectroscopy using a Bruker ESR spectrometer (ELEXSYS-II E580, USA). The concentrations of Fe element were analyzed by a Leeman Prodigy inductively coupled plasma optical emission spectroscopy (ICP-OES) system (Hudson, NH03051, USA). Confocal laser scanning microscope (CLSM) images were performed on a Zeiss LSM880 CLSM.

2.3 Synthesis of AFe nanoparticles

About 1 mL of oleylamine and 20 mL of 1-octadecene were added to a 100 mL 4-necked flask and stirred thoroughly under sufficient nitrogen atmosphere to ensure that no air remained in the

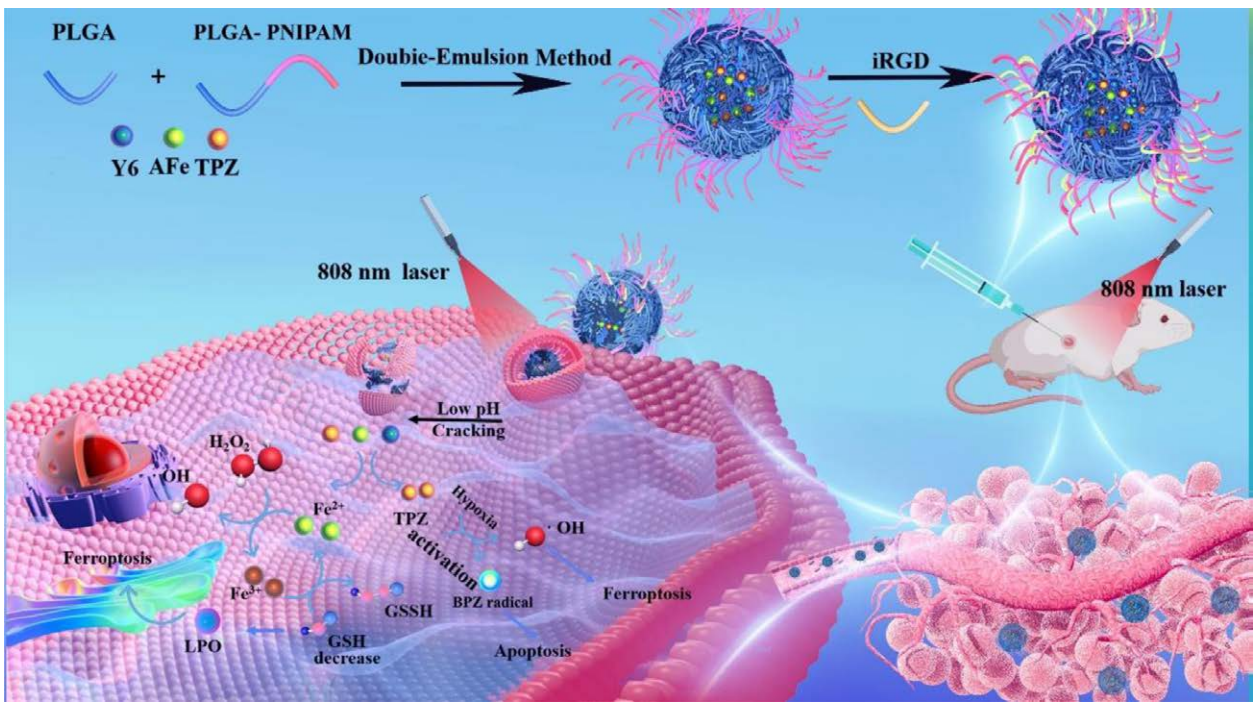

Figure 1. Schematic illustration of PP-TPZ-AFe-Y6-iRGD peptide nanocapsules formation and tumor therapeutic mechanism of PP-TPZ-AFe-Y6-iRGD nanocapsules.

system, and then this mixed solution was warmed up. At 80°C, the solution was evacuated to ensure complete removal of organic impurities. After that, 0.4 mL of Fe(CO)5 was added at 120°C, and then the temperature was raised to 180°C for 30 min. During this process, the color of the solution gradually changed from colorless to dark orange. After waiting for natural cooling to room temperature, 25 mL of acetone was added and centrifuged at 5000 rpm for 2 min, and centrifuged and washed twice to obtain black AFe nanoparticles, followed by adding 10 mL of dichloromethane (DCM) to dissolve the sample for storage.

2.4 Synthesis of PLGA-PNIPAM nanocapsules

About 1500 mg PLGA, 24 mg dicyclohexylcarbodiimide, and 23 mg *N*-hydroxy butane diimide were added to a 250 mL round-bottomed flask, followed by the addition of 50 mL of DMSO and stirring for 30 min to activate the carboxyl groups. Then, 6 mg of ethylenediamine was added to the round-bottomed flask, and the activated PLGA was slowly added dropwise to the ethylenediamine and stirred in ice bath for 24 h. After 24 h, 500 mg PNIPAM was added to the round-bottomed flask and stirred at room temperature for 24 h. After 24 h, post-treatment was carried out by extracting DMSO with ethyl acetate and water, then removing ethyl acetate by spinning, and finally adding ether to recrystallize the solution to produce a PLGA-PNIPAM solid, which was then placed in a vacuum drying oven for overnight drying and set aside.

2.5 Synthesis of PP-TPZ-AFe-Y6 nanocapsules

PLGA-PNIPAM (PP)-TPZ-AFe-Y6 nanocapsules were synthesized by microemulsion method (water/oil/water). About 100 mg PLGA-PNIPAM, 15 mg AFe nanoparticles, 8 mg Y6 molecules, and 20 mg of F127 were mixed in 3 mL of DCM. Then, 1 mL TPZ solution (20 mg/mL saline solution) was added to inject into the mixture and sonicated for 6 min (5 s on, 5 s off) using an ultrasonic probe (ultrasonic frequency: 750 W, 40%). And 10 mL of polyvinyl alcohol solution (10 mg/mL saline) was added into the mixture and sonicated for 5 min (5 s on and 5 s off) using the same ultrasonic conditions. The mixture was magnetically stirred overnight under argon protection, and then rotary evaporation was used to remove the DCM. After centrifugation for 8 min (7000 rpm), the PP-TPZ-AFe-Y6 nanocapsules were prepared by overnight drying in a freeze dryer and set aside. All processes were done under light-avoidance conditions.

2.6 Release kinetics and morphological changes of nanocapsules

Three aliquots of PP-TPZ-AFe-Y6 nanocapsules of the same mass (10 mg) were accurately weighed and dispersed in 1 mL of PBS (pH = 5.4, 6.5, and 7.4). The 3 solutions were then placed in dialysis tubing (molecular weight cutoff of 5000 Da). Then, 1 mL of dialysate was taken out at 0 h, 3 h, 6 h, 12 h, 24 h, 48 h, and 96 h, respectively. The withdrawn dialysate was diluted and filtered, and the absorbance value at 270 nm was characterized by UV–vis. It is the characteristic absorption peak of the drug molecule TPZ and can be used to calculate the cumulative release of TPZ. The concentration of iron ions in the samples was measured by ICP-OES and the cumulative release of AFe was calculated. Then the time-cumulative percent release curve was plotted by observing the drug release from PP-TPZ-AFe-Y6 nanocapsules at different pH values. In addition, to investigate the morphological changes of the drug released from the nanocapsules at different pH values, 3 samples were taken from after 12 h for TEM. In addition, in order to investigate the morphological changes of the drug released from the nanocapsules at different pH values, 3 samples were observed by TEM, respectively.

2.7 Cell culture

Murine-derived embryonic fibroblasts (NIH3T3), murine-derived breast cancer cells (4T1), and human-derived hepatocellular carcinoma cells (HepG2) cell lines were obtained from the Cancer Institute and Hospital of the Chinese Academy of Medical Science. 4T1 was cultured in RPMI 1640 medium containing 10% fetal bovine serum and 1% penicillin/streptomycin in a humidified environment at 37°C with 5% CO_2. Under the same conditions, NIH3T3 and HepG2 were cultured in Dulbecco's modified eagle medium and Eagle's minimum essential medium, respectively. All the reagents for cell culture were purchased from Invitrogen.

2.8 Clone formation experiment

The cells were digested and centrifuged while the supernatant was removed. Complete medium was added and the cells were lightly blown to suspend them evenly. After dilution, the number of cells with a cell counting plate was counted, the required volume of cells and medium was calculated, and they were mix. The mixture was added to a 6-well plate, shaken well, and placed in an incubator for 2 to 3 weeks. After the appearance of cell colonies, the medium was removed and washed twice with PBS. Afterward, 4% paraformaldehyde was added for 15 min of fixation and washed twice with PBS. Subsequently, they were stained for 30 min, and the staining solution used was crystal violet stain and washed 3 times with PBS after staining. Finally, the 6-well plate was air-dried.

2.9 Immunofluorescence

Intracellular ROS assay was measured by the ROS Assay Kit (S0033, Beyotime, China). Tumor cells were seeded into a 24-well culture plate (2×10^4 cells per well). When the cell density reached 70%, the cells were then incubated with nanocapsules for 24 h. After washing out the free nanocomposite with PBS, the fresh culture medium was added. A laser was then used to irradiate the cells for 5 min. The staining method was directed by the instructions. The cells were finally visualized using an inverted microscope (Olympus IX71).

2.10 Flow cytometry analysis

Tumor cells were seeded in 6-well plates and treated with different types of nanomedicine when the cell density reached 80% (≈10^6 cells per well). Treated cells were digested and added to a 15 mL centrifuge tube and centrifuged to remove the supernatant. It was then washed twice with phosphate buffer. The cells were resuspended with diluted DCFH-DA solution and allowed to mix thoroughly. The mixture was incubated in a carbon dioxide cell incubator at 37°C for 20 min, followed by washing tumor cells with serum-free cell culture solution 3 times. The samples were filtered using a 100 μm membrane and transferred to flow tubes. Analysis was then implemented with a cell flow cytometer.

2.11 Double staining of the live/dead cell assay

Double staining of the live/dead cell assay was carried out using the Calcein-AM/PI Double Stain Kit (40747ES76, Yeasen, Shanghai, China). 4T1 and HepG2 were seeded into a 24-well culture plate (2×10^4 cells per well). When the cell density reached 70%, the cells were then incubated with nanocapsules for 24 h. After washing out the free nanocomposite with PBS, the fresh culture medium was added. A laser was then used to irradiate the cells for 5 min. The staining method was directed by the instructions. The cells were finally visualized using an inverted microscope (Olympus IX71).

2.12 Tumor xenograft model

Balb/c mice were purchased from Guangdong Zhiyuan Biomedical Technology Co., Ltd. (Guang Zhou, China). For the tumor xenograft model, 4T1 cells (2×10^6 cells in 100 µL of saline) were injected subcutaneously into Balb/c mice at the root of the right hind legs. All animal experiments were performed according to the guidelines of the Institutional Animal Care and Use Committee of South China University of Technology, Guang Zhou, China (no. 2022090).

2.13 Grouping and administration of 4T1 tumor-bearing mice

After the tumor volume increased to about 100 mm^3, the 4T1 tumor-bearing mice were randomly divided into 6 groups, namely control group, laser group, TPZ group, PP-AFe-Y6 group, PP-TPZ-AFe-Y6-iRGD group, and PP-TPZ-AFe-Y6-iRGD + laser group. The mice were administered intratumorally on day 0. After 6 h of administration, laser irradiation (808 nm, 5 min, 1 W/cm^2) was applied to the tumor sites of mice in the laser group and PP-TPZ-AFe-Y6-iRGD + laser group; (808 nm, 5 min, 1 W/cm^2). The doses of the drug were administered at C_{Fe} = 136.2 µg/mL.

2.14 Hemolysis test

Fresh blood was obtained from female BALB/c mice at 4 to 6 weeks. Subsequently, erythrocytes (RBCs) were isolated from the plasma by dilution with PBS and the earlier steps were repeated to clarify the supernatant. The final concentration of 1% (V/V) RBCs suspension was then mixed with different concentrations of PP-TPZ-AFe-Y6. PBS and DI water were used as negative and positive controls, respectively. Next, after incubation in a water bath at 37°C for 4 h and centrifugation for 5 min, 100 µL of the supernatant of each sample was transferred to a 96-well plate. The free hemoglobin in the supernatant was measured with a microplate reader at 540 nm. The hemolysis ratio of RBCs was calculated using equation (1):

$$\text{Hemolyticratio}\,(\%) = \frac{A_{\text{sample}} - A_{\text{nagetive control}}}{A_{\text{positive control}} - A_{\text{nagetive control}}} \times 100\% \quad (1)$$

where A_{sample}, $A_{negative\ control}$, and $A_{positive\ control}$ were denoted as the absorbance of sample, negative and positive control, respectively.

2.15 Statistical analysis

Results were presented as means ± standard deviation. Student 2-tailed nonpaired *t* test was used to determine the significance between treatment and control groups in all experiments. $P < 0.05$ was considered statistically significant; $^*P < 0.05$, $^{**}P < 0.01$ and n.s. indicates no significant difference.

3. Result and discussion

3.1 Synthesis and characterization

Initially, we successfully synthesized AFe nanoparticles utilizing a hydrothermal method with $Fe(CO)_5$ as the precursor. TEM images showed good homogeneity and dispersion of the AFe particles. Their average diameter was about 8 nm by particle size analysis (Figure 2A, B). Subsequently, we synthesized the temperature- and acid-responsive multiblock polymer PLGA-PNIPAM via an amidation reaction. The formation of amide bonds was confirmed by Fourier infrared spectroscopy characterization (Supplementary Figures S1 and S2, http://links.lww.com/MEDMAT/A1). Finally, we succeeded in preparing PP-TPZ-AFe-Y6 nanocarriers by employing the microemulsion method, which effectively introduced hydrophobic AFe and hydrophilic TPZ into PLGA-PNIPAM nanocarriers to realize the synergistic encapsulation of multicomponents. After the evaporation of organic solvents, the PP-TPZ-AFe-Y6 nanocapsules were obtained by centrifugal purification (Figure 1). To verify the stability of the nanocapsules, they were dissolved in water for 14 days, and the hydration kinetic diameters and zeta potentials of the nanocarriers hardly changed with time, which proved that the nanocarriers were well stabilized in aqueous solution (Figure 2C). XRD spectroscopy analysis reveals the crystal structure of iron nanoparticles: the amorphous state of Fe (Figure 2E). The UV absorption peak at around 265 nm proved that the nanocarriers were successfully loaded with TPZ (Figure 2F). Elemental mapping images of PP-TPZ-AFe-Y6 were provided to show the presence of Fe, F, and S in the nanocarriers more intuitively, indicating that AFe and Y6 molecules were successfully loaded inside the nanocarriers (Figure 2D and Supplementary Figure S3, http://links.lww.com/MEDMAT/A1). The existence of Fe 2p peaks in X-ray photoelectron spectroscopy (XPS) suggests the availability appearance of Fe^{2+}, supporting the presence of a ferrous oxide phase in AFe nanoparticles (Figure 2G and Supplementary Figure S4, http://links.lww.com/MEDMAT/A1). Combined with XPS map analysis of AFe, AFe nanoparticles showed no significant changes after complexation with PP-TPZ-AFe-Y6 nanocapsules (Supplementary Figure S5a, b, http://links.lww.com/MEDMAT/A1). The Zeta potential analysis verified that PP-TPZ-AFe-Y6 nanocapsules, with a hydration kinetic diameter of approximately 230 nm, were able to efficiently deliver therapeutic mediator to the tumor region through the enhanced permeability and retention (EPR) effect (Supplementary Figure S6a, http://links.lww.com/MEDMAT/A1), essential for achieving favorable treatments. In addition, the modification of tumor-homing and penetrating peptide (iRGD) markedly reduced the electronegativity of the nanocarrier, which could effectively improve the feeding of tumor cells into the nanocarrier (Supplementary Figure S6b, http://links.lww.com/MEDMAT/A1). In summary, we succeeded in synthesizing a nanodrug delivery system with good stability, laying a prerequisite for subsequent biological validation.

3.2 Responsive degradation behavior of nanocapsules

We evaluate the rate and mechanism of release of nanocapsules under specific conditions, ensuring that the drug will achieve the desired therapeutic effect in vivo. We simulated the degradation

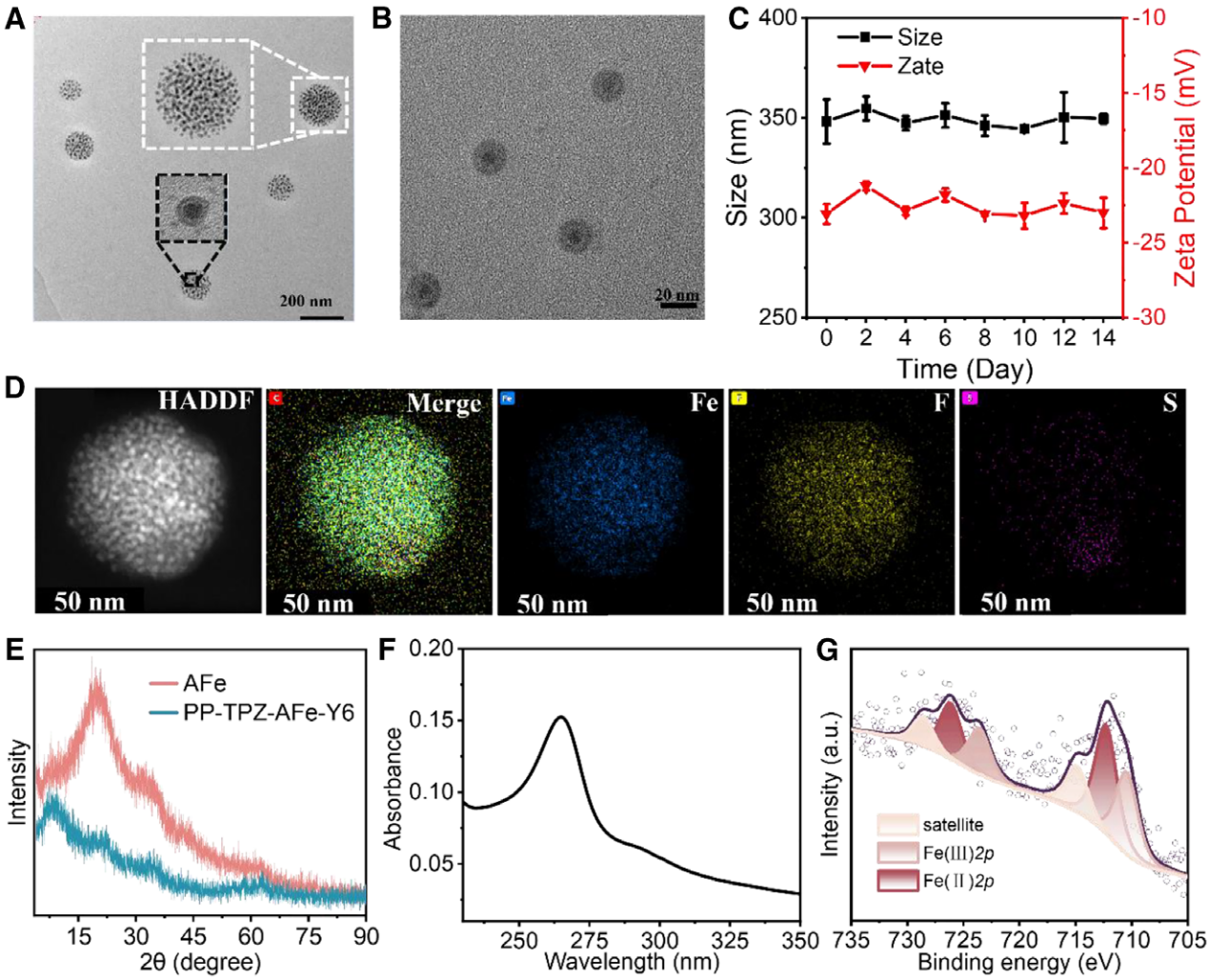

Figure 2. Synthesis and characterization of PP-TPZ-AFe-Y6 nanocapsules. (A) TEM image of PP-TPZ-AFe-Y6 nanocapsules; (B) TEM image of AFe nanoparticles; (C) stability of PP-TPZ-AFe-Y6 nanocapsules in water; (D) elemental distribution of PP-TPZ-AFe-Y6 nanocapsules; (E) XRD image of AFe nanoparticles and PP-TPZ-AFe-Y6 nanocapsules; (F) UV–vis spectra of PP-TPZ-AFe-Y6 nanocapsules; (G) high-resolution XPS maps of Fe 2p of PP-TPZ-AFe-Y6 nanocapsules; Scale bar: 20 nm, 50 nm, and 200 nm.

behavior of nanocapsules under different physiological environments. Under laser irradiation, Y6 molecule absorbs optical energy and excites the state through the electron transition, resulting in an increase in their internal energy. Subsequently, the molecules release energy via nonradiative pathways, converting this energy into thermal energy, which subsequently increases the temperature. Therefore, we investigated the conditions for optimal photothermal efficiency of PP-TPZ-AFe-Y6 nanocapsules under 808 nm laser irradiation. The optimized conditions were obtained as follows: the concentration of the nanocapsules: 100 mg/L, the laser power: 1 W/cm^2, the irradiation time: 5 min, and the temperature change: approximately 13°C. (Supplementary Figure S7a, b, http://links.lww.com/MEDMAT/A1). Of note, nanocapsules maintain excellent photothermal effect even after 4 irradiation cycles (Supplementary Figure S7c, http://links.lww.com/MEDMAT/A1). Then, we dispersed the nanocapsules in PBS with different pH to simulate the faintly acidic tumor microenvironment. The photothermal effect within the tumor was simulated by setting a temperature environment of 43°C, then we evaluated the acid-responsive degradation of the nanocapsules under thermally stimulated conditions. In solution at pH 7.4, the nanocapsules remained stable for 12 h, showing excellent stability under physiological conditions; at pH 6.5, the nanocapsules showed minor cleavage for 12 h; in pH 5.4 buffer, the nanocapsules exhibited pronounced cleavage leading to the release of AFe nanoparticles, presenting an acid-sensitive degradation process (Figure 3A). The acid-responsive degradation behavior was attributed to the breaking of ester bonds in PLGA at pH below 6.5. Meanwhile, the thermal sensitivity of PNIPAM caused changes in the structure of the nanocapsules as the temperature increased, further promoting nanocapsules degradation. Our design takes advantage of the favorable photothermal effect of the nanocapsules and combines it with the acid-responsive degradation properties in the microenvironment of tumors to achieve more precise and effective drug release, thus improving therapeutic efficacy and reducing side effects. Subsequently, the kinetics of TPZ and AFe release from PP-TPZ-AFe-Y6 nanocapsules were tested under different stimulation conditions. Furthermore, based on standard curves of TPZ (Figure 3B and Supplementary Figure S8, http://links.lww.com/MEDMAT/A1), we specifically analyzed the drug release over 96 h under different pH (7.4, 6.5, and 5.4) and temperature (25°C, 37°C, and 45°C) conditions. At 43°C, the release rates of TPZ were 73% (pH 7.4), 84% (pH 6.5), and 90% (pH 5.4), and that of AFe

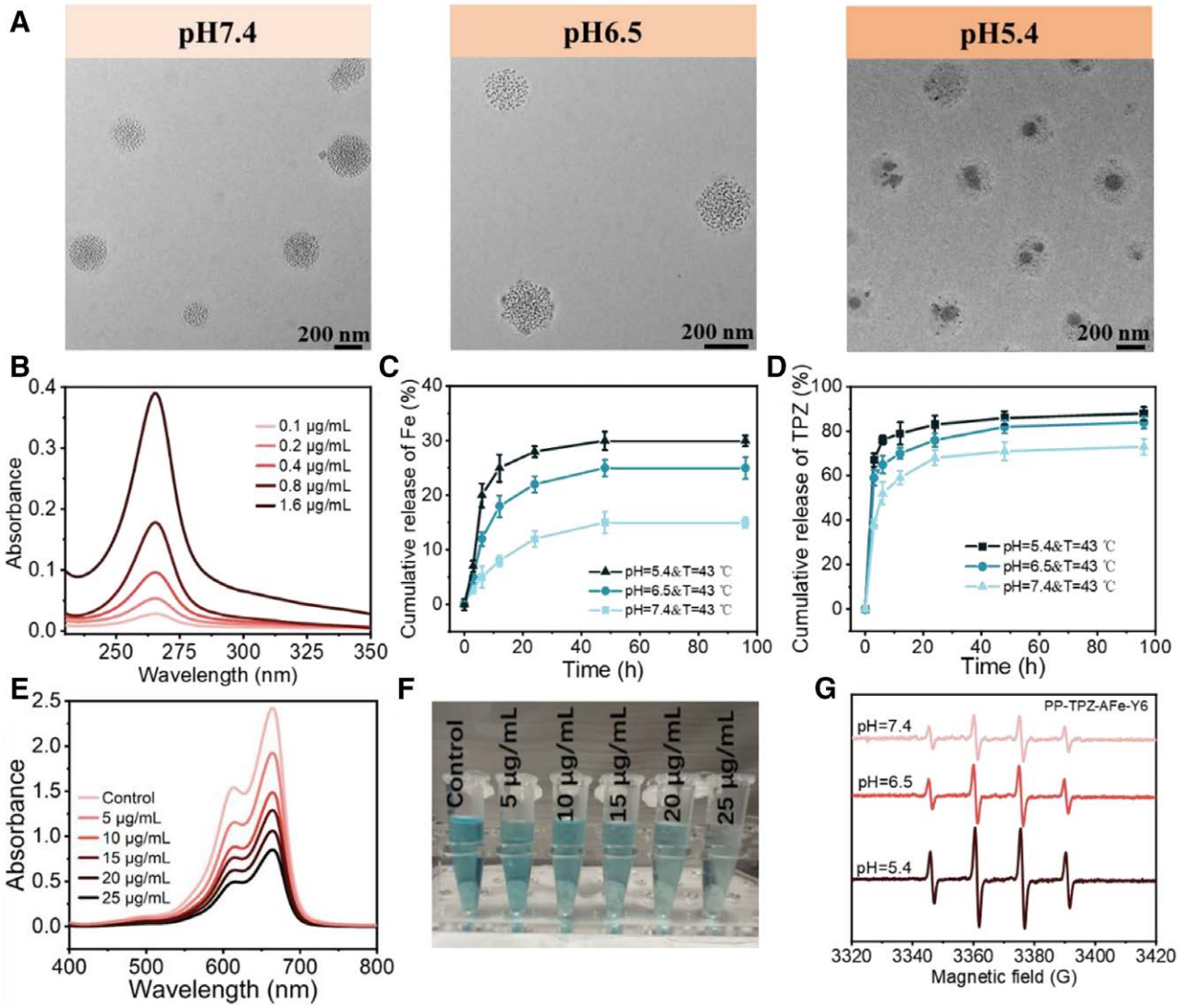

Figure 3. Stimulus-responsive degradation of PP-TPZ-AFe-Y6 nanocapsules. (A) TEM images of PP-TPZ-AFe-Y6 nanocapsules dispersed in different pH buffers; (B) UV–vis spectrograms of different concentrations of TPZ solutions; cumulative release rates of (C) AFe and (D) TPZ from PP-TPZ-AFe-Y6 nanocapsules in different pH buffers; (E) UV–vis spectrograms and (F) photographs of different concentrations of PP-TPZ-AFe-Y6 nanocapsules assayed to produce ROS in UV–vis spectrograms; (G) ESR spectra of PP-TPZ-AFe-Y6 nanocapsules after treatment with different pH buffer solutions.

were 15% (pH 7.4), 25% (pH 6.5), and 30% (pH 5.4), respectively. At pH 7.4, the release rates of TPZ and AFe were the lowest, indicating that the drugs could be effectively retained under normal physiological conditions (Figure 3C, D). The main reason for the lower release rate of AFe than TPZ is that iron-based nanomaterials possess more stability and a slower degradation rate, and these material properties determine a slower release rate than that of chemotherapeutic drugs. The release of TPZ and AFe from the nanocapsules showed a pH dependence: the release profiles of TPZ and AFe were significantly elevated under acidic conditions. At pH 5.4, the release rates of TPZ were 45% (25°C), 49% (37°C), and 90% (45°C), respectively, and that of Fe were 5% (25°C), 20% (37°C), and 30% (45°C), respectively, at pH 5.4 (Supplementary Figure S9a, b, http://links.lww.com/MEDMAT/A1). These results demonstrate that PP-TPZ-AFe-Y6 nanocapsules are capable of achieving effective and controlled release of TPZ and AFe under acidic and photothermal conditions. The PP-TPZ-AFe-Y6 nanocapsules exhibited significant acid- and photothermal-responsive degradation properties due to the acid sensitivity of PLGA, the thermosensitivity of PNIPAM, and the photothermal effect of Y6 molecules. The exploration of Fe^{2+} in nanocarriers has attracted much attention in recent years due to inducing the high-efficiency Fenton reaction, which has rendered it a classic component of nanocomposites. As a novel reagent for the Fenton reaction, the AFe released from nanocapsules was able to generate large amounts of ROS in tumor cells.[21–25] Simultaneously, we verified the participation of AFe released from nanocarriers in the Fenton reaction under different conditions. The experimental results suggested that the degradation rate of methylene blue (MB) was the highest in the PP-TPZ-AFe-Y6 + laser group (Supplementary Figure S10, http://links.lww.com/MEDMAT/A1). With the concentration of PP-TPZ-AFe-Y6 increases, more ·OH could be produced, causing substantial MB degradation (Figure 3E, F). We further confirmed the generation of ·OH by electron spin resonance (ESR) test, whose profile showed 4 characteristic peaks of ·OH. The 4 characteristic peaks of ·OH with a typical 1:1:1:1 signal were the strongest at pH 5.4, which provided support for the highly efficient ROS generation ability of PP-TPZ-AFe-Y6 nanocapsules in acidic environments (Figure 3G and Supplementary Figure

S11, http://links.lww.com/MEDMAT/A1). The aforementioned experimental results suggest that PP-TPZ-AFe-Y6 nanocapsules are capable of achieving controlled release of drug and AFe under acidic and photothermal conditions, together with producing a large amount of ROS in the faintly acidic tumor microenvironment through the Fenton reaction, which provides feasibility to inhibit the proliferation of tumor cells.

3.3 Evaluation of in vitro antitumor effects

In order to ensure that the nanocapsules have good biosafety in inhibiting tumor cell proliferation, we initially evaluated the biotoxicity of different concentrations of PLGA-PNIPAM and the duration of interaction on various cell lines. The test results suggested that the survival rate of the cell lines all reached up to 90%, confirming the good biosafety of PLGA-PNIPAM nanocarriers (Figure 4A, B). To further investigate the cell-killing effect of nanocapsules stimulated by external conditions, we coincubated different concentrations of PP-TPZ-AFe-Y6 nanocapsules with NIH3T3, 4T1, and HepG2, respectively, and subjected the corresponding groups to laser irradiation treatment. As the concentration of PP-TPZ-AFe-Y6 nanocapsules reached a relatively high concentration of 100 mg/mL, the survival rate of NIH3T3 still remained above 90%. The toxicity of PP-TPZ-AFe-Y6 nanocapsules to NIH3T3 was almost negligible, which proved that it carried out good biosafety for normal cells. The viability of the treated 4T1 and HepG2 was significantly reduced, showing concentration dependence (Supplementary Figure S12, http://links.lww.com/MEDMAT/A1). The above experimental results show that PP-TPZ-AFe-Y6 nanocapsules are able to

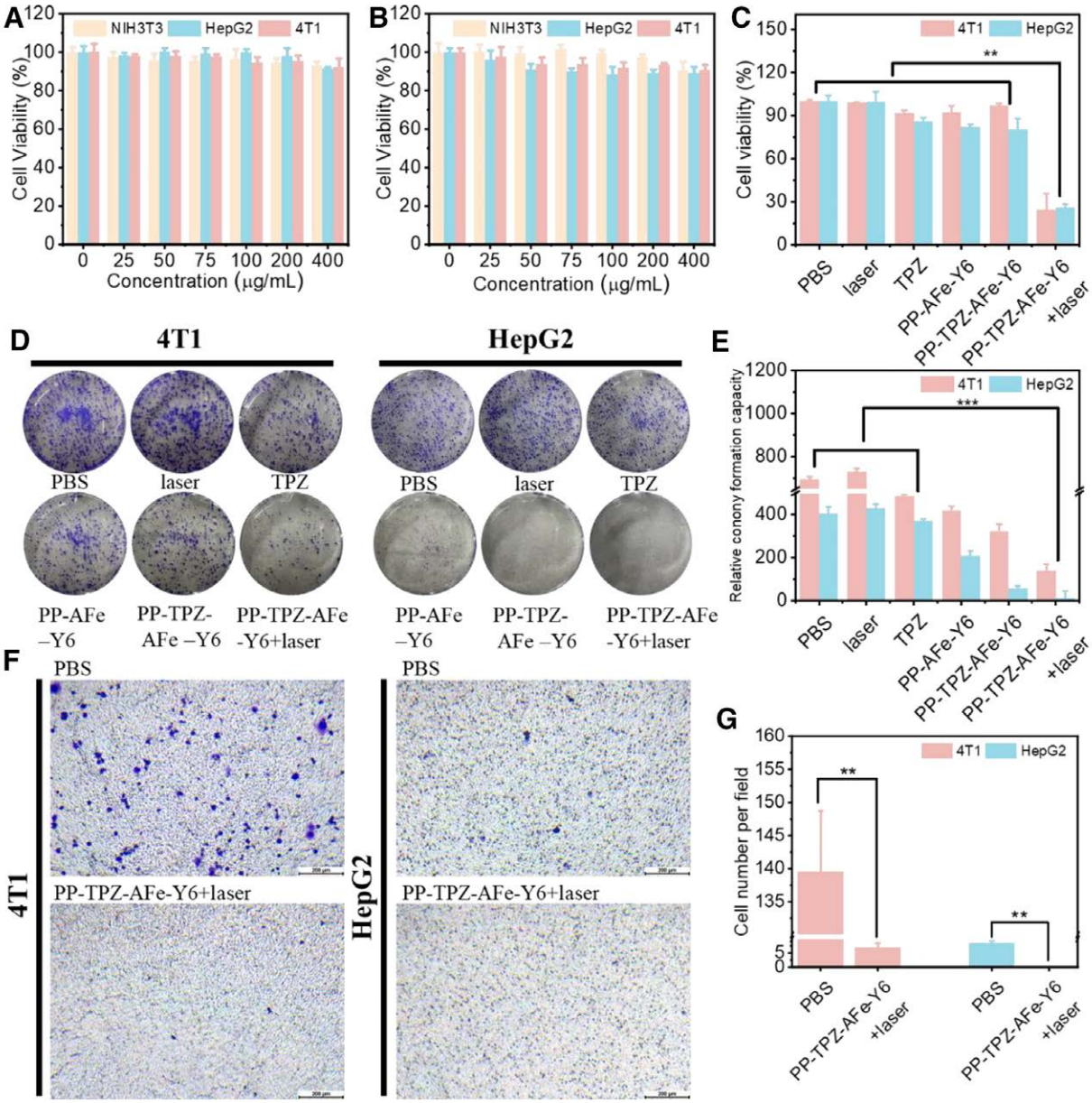

Figure 4. Evaluation of cell proliferation effects in vitro. Cell viability of NIH3T3, HepG2, and 4T1 after treatment with PLGA-PNIPAM nanocapsules for (A) 24 h and (B) 48 h; (C) cell viability of 4T1 and HepG2 after different treatments; (D) representative images of monolayer colony formation assay for 4T1 and HepG2 after different treatments and (E) quantitative results; (F) representative pictures and (G) quantitative results of Transwell experiments after different treatments; scale bar: 200 μm; laser parameters in the experiments: 808 nm, 1.0 W/cm^2 and 5 min. *P < 0.05 vs PBS, **P < 0.01 vs PBS,***P < 0.001 vs PBS.

achieve efficient treatment of tumor cells under external stimulation conditions without damaging normal cells. Subsequently, we investigated the effect of different components of the nanocarriers on tumor cell viability. Subsequently, we investigated the effects of different components of the nanocarriers on tumor cell viability. Laser, TPZ, PP-AFe-Y6, PP-TPZ-AFe-Y6, and PBS groups showed no apparent change in cell viability, which was above 90%. Nevertheless, under laser irradiation, the cell viability of the PP-TPZ-AFe-Y6 group dramatically decreased to below 30% (Figure 4C). This result was attributed to the fact that laser irradiation promoted the degradation of the nanocapsules, releasing the internally loaded TPZ and AFe, which significantly inhibited the proliferation of tumor cells. We further validated the influence of tumor stem cells and tumor cell migration ability through plate cloning and cell migration assays. The results of plate cloning experiments showed that there was no significant difference in the proliferation ability of cell stem cells under PBS and other treatment conditions, whose colony clusters were relatively great. In contrast, PP-TPZ-AFe-Y6 nanocapsules effectively inhibited the clone formation of tumor cells under laser irradiation, confirming that PP-TPZ-AFe-Y6 nanocapsules coupled with laser treatment significantly suppressed the proliferation of tumor stem cells (Figure 4D, E). The results of the wounding heal revealed that PP-TPZ-AFe-Y6 was capable of effectively reducing the migratory ability of 4T1 upon laser irradiation (Supplementary Figure S14a, c, http://links.lww.com/MEDMAT/A1). The inhibitory effect of nanocapsules on the migration ability of HepG2 is not significant because of its weaker migration ability (Supplementary Figure S14b, d, http://links.lww.com/MEDMAT/A1). The results of transwell experiments had little controversy in conclusions (Figure 4F, G). The foregoing experimental results suggest that the synthesized nanocapsules not only have good biocompatibility but also can inhibit the relevant phenotypes of tumor cells, providing a solid foundation for following biological experiments.

3.4 Tumor cell internalization

Internalization of nanomaterials by cancer cells plays a crucial role in inducing changes in cellular behaviors that may dictate the efficiency of cancer therapy. To assess the uptake ability of tumor cells to the nanocapsules, we incubated the Cy3-labeled PP-TPZ-AFe-Y6 with 4T1 and HepG2 for 2 h and 8 h, respectively. Under the same concentration of PP-TPZ-AFe-Y6 nanocapsules, the uptake of nanocapsules by 4T1 and HepG2 increased from 1.19% and 0.62% to 17.2% and 28.5%, respectively (Figure 5A, B). The test results show that tumor cells are more likely to phagocytose more nanocapsules at longer incubation times, which is critical for the effectiveness of drug delivery. Hydroxyl radicals, being highly reactive free radicals, are capable of oxidizing mitochondrial membrane lipids and proteins and disrupting mitochondrial structure and function, which lead to disorders of cellular energy metabolism and the onset of apoptosis.[26] We observed the morphology of tumor cell mitochondria by biological TEM to assess the cellular damage induced by hydroxyl radical. As shown in Figure 5C, the mitochondria in the PBS group were structurally intact with clear cristae. In cells treated with PP-TPZ-AFe-Y6 nanocapsules and laser, the generated ·OH increased the intracellular oxidative stress level (ROS), leading to mitochondrial membrane LPO, membrane structure disruption, and cristae disintegration. The nanocapsules caused significant damage to mitochondria after light treatment.[26,27] The results of live/dead cell fluorescence staining experiments showed that compared with other parallel experimental groups, PP-TPZ-AFe-Y6 + laser resulted in a relatively great quantity of cell death, displaying a significant cytotoxic effect (Figure 5D, E). The findings of the abovementioned experiments exhibit that PP-TPZ-AFe-Y6 nanocapsules possess a strong killing ability on tumor cells under laser irradiation.

3.5 Efficiency of ROS generation in vitro

Cell survival is markedly affected by ROS, and high levels of ROS are capable of inducing apoptosis and necrosis because of cell membrane LPO, protein oxidation, and DNA damage.[28–30] Via ROS fluorescent probe (DCFH-DA), we detected the intracellular ROS level triggered by different components of the nanocapsules. The green fluorescent signal of 2',7'-dichlorofluorescein (DCF) was the most pronounced in the PP-TPZ-AFe-Y6 + laser group, which indicated that there was a higher oxidative stress level in the tumor cells, suggesting that the laser-irradiated nanocapsules have excellent ROS generation ability in the tumor cells (Figure 6A, B). Subsequently, we analyzed the influences of different treatment conditions on tumor cell apoptosis by flow cytometry. 4T1 and HepG2 exhibited higher apoptosis and necrosis ratios (21.8% and 30.55%) in the PP-TPZ-AFe-Y6 + laser group, respectively (Figure 6C, D, and Supplementary Figure S13, http://links.lww.com/MEDMAT/A1). The mentioned experimental results indicated that the combination of apoptosis and nonapoptosis tumor death modality would provide an avenue for tumor therapy.

The ROS-glutathione (GSH)-malondialdehyde (MDA)-LPO axis is recognized as an important pathway for ferroptosis. Intracellular ROS deplete GSH, and the decrease in GSH levels leads to lower activity of GPX4, which increases the production of LPO and MDA, ultimately promoting ferroptosis.[31–34] For this reason, we explored the therapeutic mechanism of PP-TPZ-AFe-Y6 on tumors under photothermal conditions. Initially, the intracellular GSH content under different treatment conditions was measured and analyzed. The experimental results displayed that under laser irradiation conditions, the nanocapsules released loaded AFe to generate ·OH via the Fenton reaction, which consumed a large amount of intracellular GSH in the tumor cells (Figure 6E). Then, we investigated the levels of MDA, a typical end product of LPO decomposition, in tumor cells under different treatment conditions. The reaction product of MDA and thiobarbituric acid absorbs strongly at 532 nm, which is used to quantify intracellular MDA levels.[35] The results revealed that the PP-TPZ-AFe-Y6 group presented a significant increase in the content of MDA under laser irradiation compared with another parallel group (Figure 6F). The combined effect of this multiple mechanism made PP-TPZ-AFe-Y6 nanocapsules exhibit strong GSH consumption and MDA generation abilities under laser irradiation, which hindered the elimination of LPO, thus significantly increasing the intracellular ROS level and exacerbating the process of ferroptosis in tumor cells. In conclusion, the PP-TPZ-AFe-Y6 nanocapsules were found to effectively destroy tumor cells through multiple mechanisms after NIR laser treatment. This undesirable destructive process can become a novel tool applicable to cancer treatment.

3.6 Evaluation of biosafety and tumor therapy in vivo

In vitro experiments, we observed significant tumor cell-killing effects of the nanocapsules. To deepen the study of the

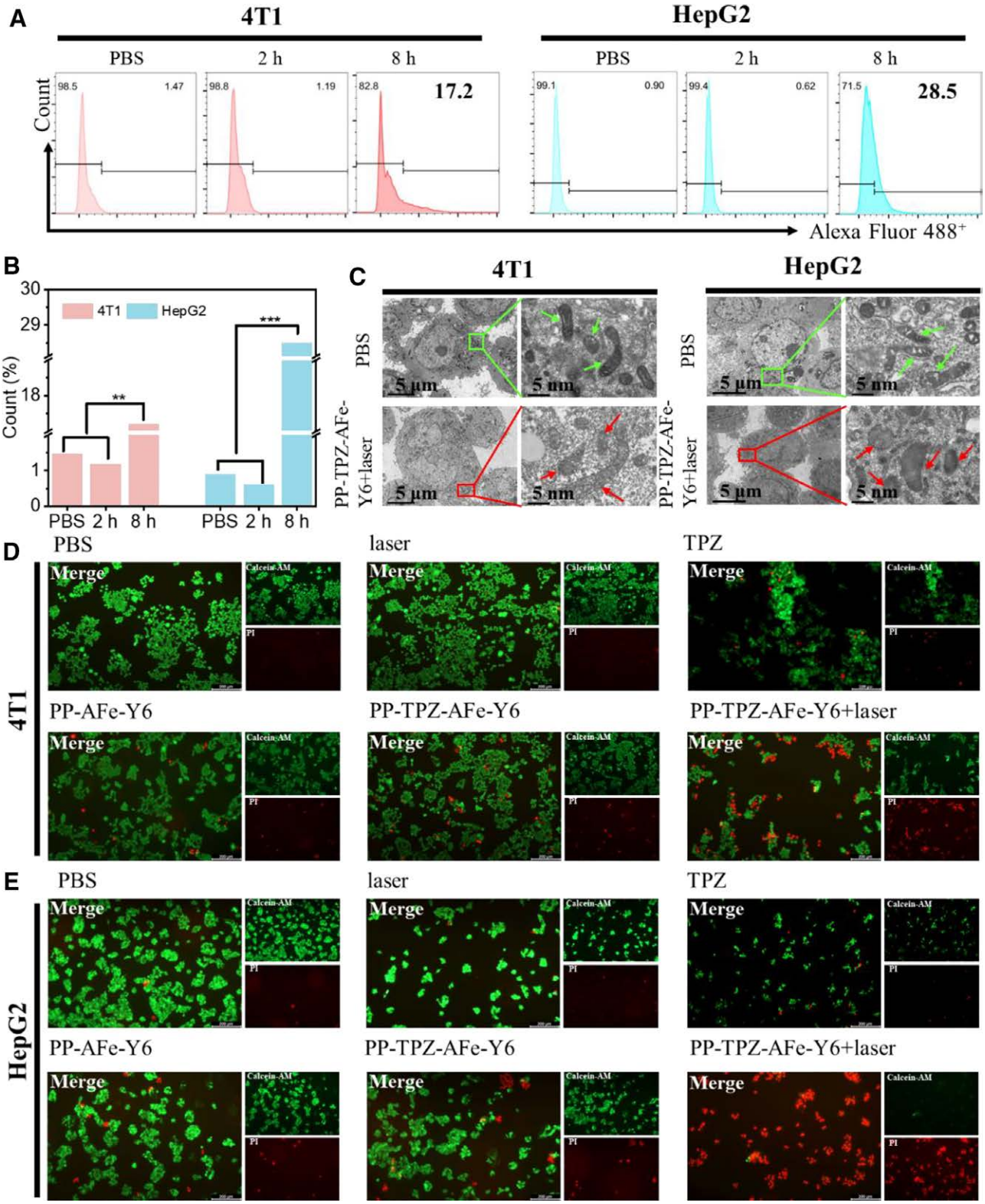

Figure 5. Evaluation of cellular antitumor effects in vitro. (A) Uptake of PP-TPZ-AFe-Y6-Cy3 nanocapsules by 4T1 and HepG2 at different times and (B) quantitative results; (C) Bio-TEM images of cross-sections of 4T1 and HepG2 after different treatments, with green arrows denoting normal mitochondria and red arrows denoting mitochondria damage; fluorescence images of (D) 4T1 and (E) HepG2 stained with Calcein-AM (live cells, green fluorescence) and PI (dead cells, red fluorescence) staining of fluorescence images of (D) 4T1 and (E) HepG2; Scale bar: 200 μm, 5 μm, and 5 nm; Laser parameters in the experiments were 808 nm, 1.0 W/cm^2, and 5 min, respectively. *$P < 0.05$ vs PBS, **$P < 0.01$ vs PBS, ***$P < 0.001$ vs PBS..

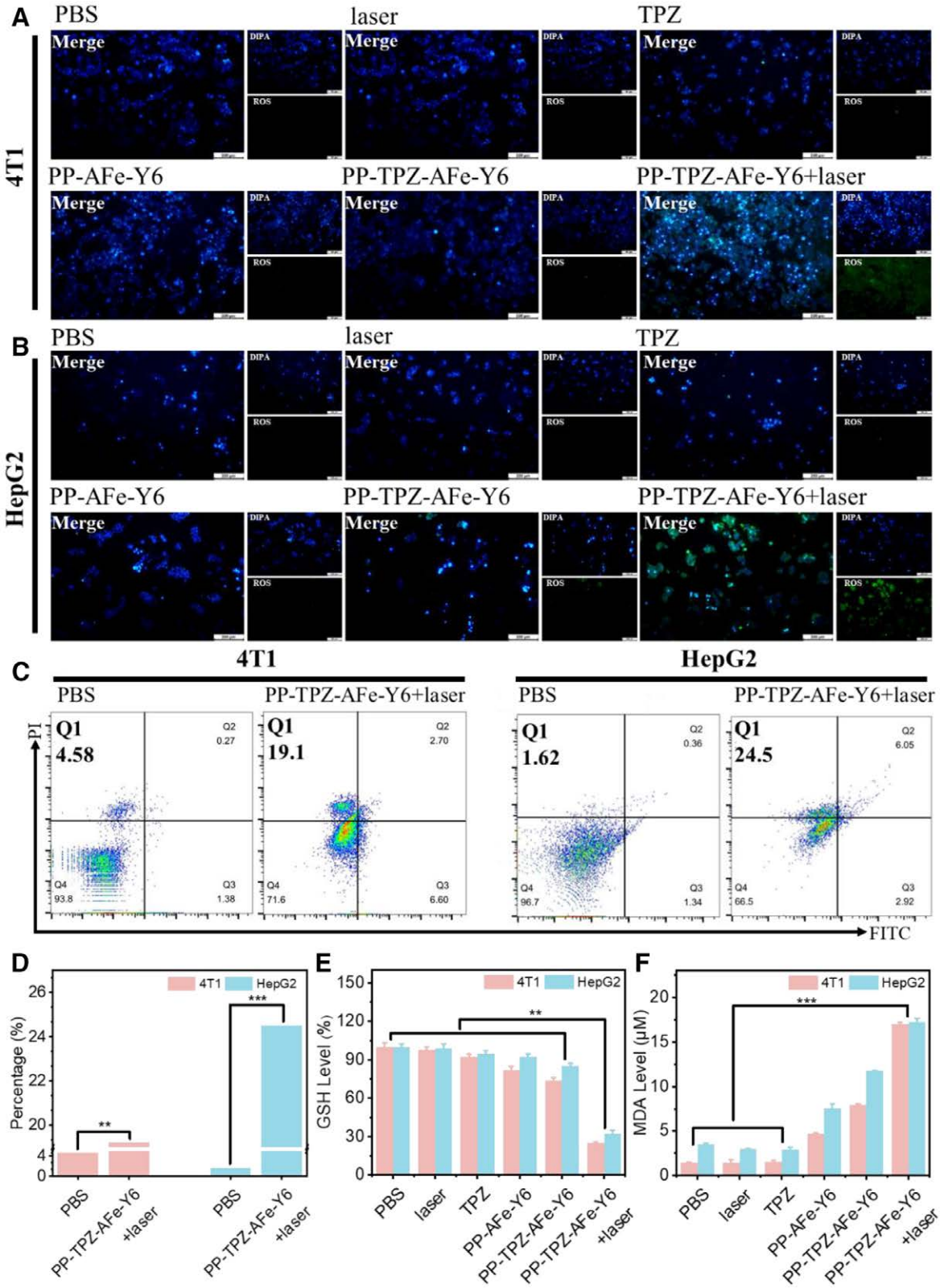

Figure 6. Exploration of cell-killing mechanism in vitro. ROS levels in (A) 4T1 and (B) HepG2 after different treatments, the blue color represents nuclei stained with diisopropanolamine and green color represents generated ROS; (C) results of apoptosis and necrosis experiments and (D) quantitative results of 4T1 and HepG2 after different treatments; (E) GSH levels and (F) MDA levels of 4T1 and HepG2 after different treatments; scale bar: 200 μ m; laser parameters in the experiment were 808 nm, 1.0 W/cm^2, and 5 min. *P < 0.05 vs PBS, **P < 0.01 vs PBS,***P < 0.001 vs PBS.

therapeutic effects of PP-TPZ-AFe-Y6-iRGD nanocapsules in vivo, we first loaded the NIR fluorescent molecule, Indocyanine green (ICG), into these nanocapsules and tracked their diffusion and distribution in mice, aiming to explore the nanocapsules' ability of targeting and recognizing the tumor. As shown in Figure 7A, PP-TPZ-AFe-Y6-ICG-iRGD nanocapsules showed

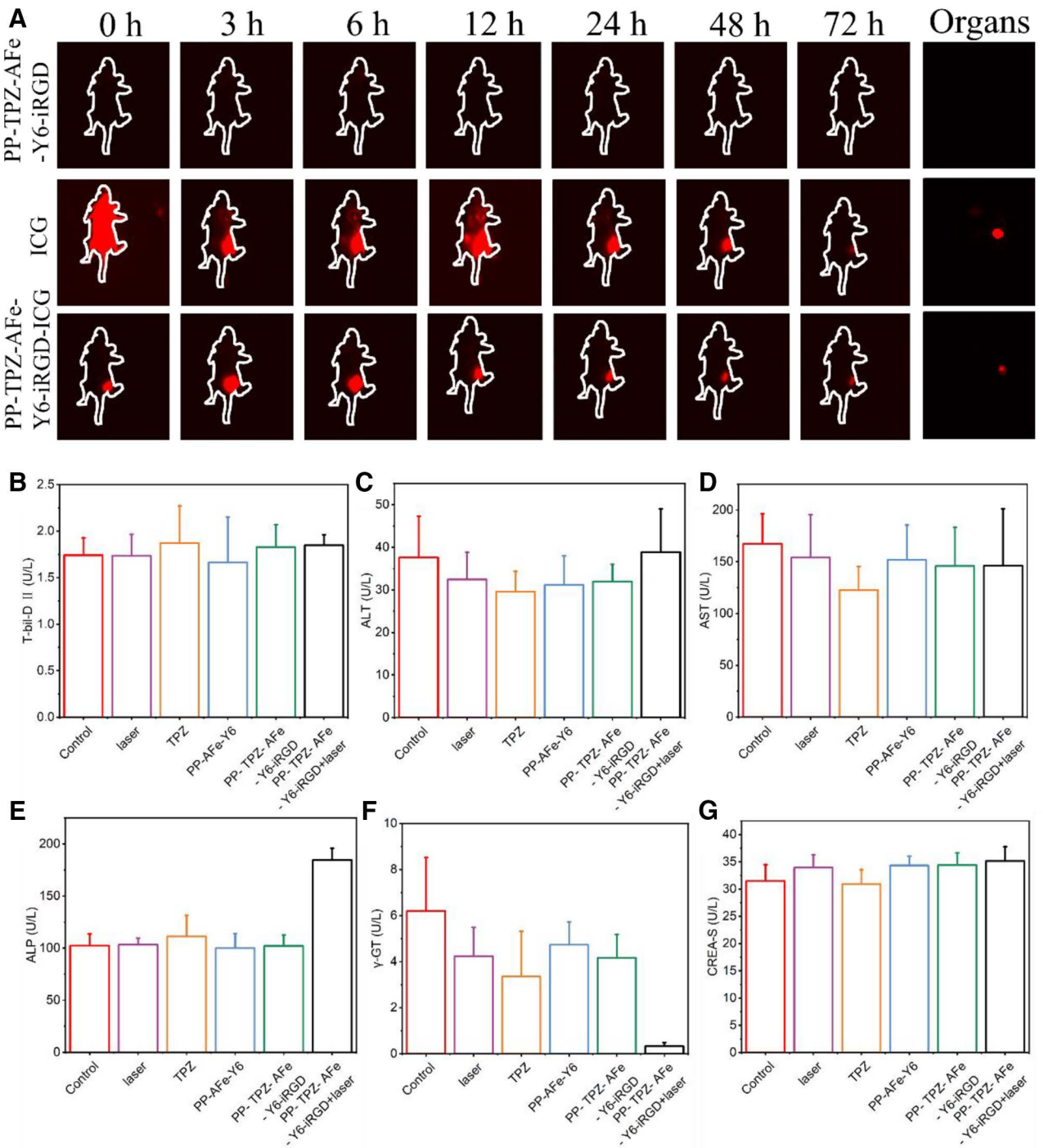

Figure 7. In vivo imaging and biosafety evaluation. (A) NIR-II fluorescence images of 4T1 tumor-bearing mice at different times; variations of blood biochemical indices of (B) T-bil-D II, (C) ALT, (D) AST, (E) ALP, (F) γ-GT and (G) serum creatinine (CREA-S) in each group of mice at the end of treatment.

excellent target recognition ability for tumors. The fluorescence intensity of ICG at the tumor site peaked at about 6 h after intratumoral administration, which proved that the nanocapsules were well enriched and uniformly distributed at the tumor loci. As a result, laser irradiation at about 6 h of drug administration was able to achieve the desired therapeutic effect. In contrast to the nonspecific distribution in the ICG group, the fluorescence of the nanocapsules was capable of sustained enrichment at the tumor loci after 72 h of administration without spreading to other parts of the mice. These experimental results suggest that PP-TPZ-AFe-Y6-ICG-iRGD nanocapsules have good bio-targeting properties to tumor tissues, conducive to reducing the toxicity of drug molecules in vivo and improving the safety of treatment.

After that, we investigated the biosafety and tumor elimination ability of PP-TPZ-AFe-Y6-iRGD nanocapsules in 4T1 tumor-bearing mice. The mice were divided into 6 groups: control (PBS), laser, TPZ, PP-AFe-Y6, PP-TPZ-AFe-Y6-iRGD, and PP-TPZ-AFe-Y6-iRGD + laser. The mice in each group were injected with nanocapsules in the tumor region for 6 h and then irradiated with a NIR laser (Figure 8A). All groups of mice exhibit a steady increase in body weight throughout

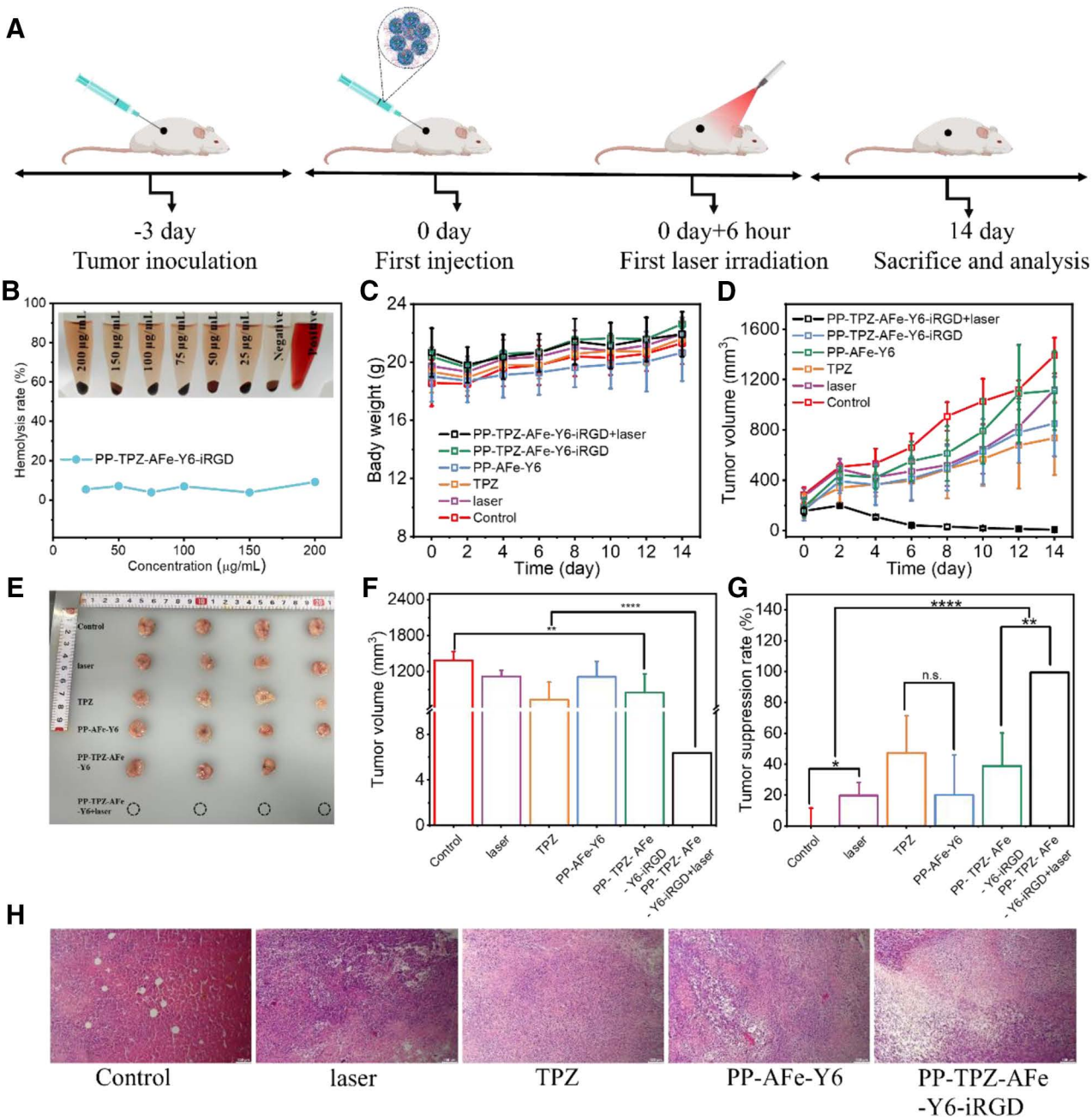

Figure 8. In vivo therapeutic effects of PP-TPZ-AFe-Y6-iRGD nanocapsules. (A) Treatment scheme of 4T1 tumor-bearing mice; (B) hemolysis assay of mouse erythrocytes incubated with different concentrations of PP-TPZ-AFe-Y6-iRGD nanocapsules, with PBS and purified water serving as the negative and positive controls, respectively; (C) body weight growth curves of the mice in each group; (D) tumor growth curves of the mice in each group; (E) histograms of the isolated tumor tissues of the mice in each group; (F) tumor volume histogram of each group of mice; (G) tumor inhibition rate of each group of mice; (H) H&E staining results of tumor tissues of each group of mice at the end of the treatment; Scale bar: 100 μm. *P < 0.05 vs PBS, **P < 0.01 vs PBS, ***P < 0.001 vs PBS,****P < 0.0001 vs PBS.

the treatment (Figure 8C), exhibiting that there is little effect on the growth and health of tumor-bearing mice. Mouse blood biochemical index assays were used to further evaluate the effect of PP-TPZ-AFe-Y6-iRGD nanocapsules on biosafety. As shown in Figure 7B–G, PP-TPZ-AFe-Y6-iRGD nanocapsules did not induce significant variations in liver function indices including alanine aminotransferase (ALT), alanine oxaloacetate aminotransferase (AST), alanine alkaline phosphatase (ALP), and triglyceride (γ-GT), as well as renal function indices such as bilirubin (T-bil-D II), and serum albumin (ALB II), in mice. Biochemical tests were all within the normal range, suggesting that no obvious infection or inflammation was triggered during the treatment period. Although the γ-GT index in the PP-TPZ-AFe-Y6-iRGD + laser group was smaller than that in the other treatment groups, it was above zero, but its level was still within the safe range. The results of hemolysis experiments demonstrated that the nanocapsules did not damage the erythrocytes significantly when circulating in vivo, displaying superior biocompatibility (Figure 8B). The aforementioned results proved that PP-TPZ-AFe-Y6-iRGD does not cause functional damage to major organs in vivo, and possesses favorable biosafety.

In contrast, there was a significant difference in tumor volume among the different treatment groups. Compared with the control and laser groups, the tumor growth trajectories of the PP-AFe-Y6 and PP-TPZ-AFe-Y6-iRGD groups were slightly affected, the tumor growth of the TPZ group was significantly inhibited, and the PP-TPZ-AFe-Y6-iRGD + laser group showed the most significant reduction in tumor volume and even achieved complete elimination of tumors, which indicated that the joint action of TPZ and ferroptosis achieved the inhibition of tumor tissue growth (Figure 8D, F). At the end of the treatment, tumor tissues from each group of mice were collected and photographed and the tumor inhibition rate was calculated. The experimental data further confirmed the significant tumor-eliminating ability of PP-TPZ-AFe-Y6-iRGD under laser irradiation (Figure 8E, G). In addition, the changes in the morphology of tumor tissues in each treatment group were observed by staining with hematoxylin and eosin (H&E). It was found that the morphology of tumor tissues in each treatment group appeared to be altered to different degrees. The number and density of cells in the tumor tissues of the TPZ group, the PP-AFe-Y6 group, and the PP-TPZ-AFe-Y6-iRGD group appeared to be significantly reduced relative to those in the control group and the laser group, proving its significant inhibitory effect on the growth of tumor tissues (Figure 8H). There were no staining results of tumor tissues in the PP-TPZ-AFe-Y6-iRGD + laser group because of the elimination of tumor tissues. We collected the main organs (spleen, liver, lung, kidney, and heart) of mice in different treatment groups for assessing the toxicity of PP-TPZ-AFe-Y6-iRGD nanocapsules in vivo by H&E staining. The results are shown in Supplementary Figure S15, http://links.lww.com/MEDMAT/A1, suggesting that the organs of the mice in each treatment group were well-morphologized with no significant variations. PP-TPZ-AFe-Y6-iRGD demonstrated excellent biocompatibility as well as significant inhibition of tumor cell proliferation both in vivo and in vitro experiments. Thus, the designed nanocapsules present great potential to be robust and versatile remedial nanoplatforms with minimal toxicity and high potency for tumor therapy.

4. Conclusion

As cancerous issues are gradually threatening the survival and health of human beings, the bottleneck of traditional treatments is forcing medical researchers to explore novel treatments. The emergence of nanomaterials provides ideas for the exploration of tumor therapeutic means. Ferroptosis, a newly discovered cell death mechanism, can not only effectively eradicate cancer cells but also overcome the drug resistance problem inherent in traditional treatments. Meanwhile, smart nanomedicine delivery systems improve tumor therapeutic effects by improving drug targeting, controlled release, and reducing side effects. The combination of them exhibits massive potential for clinical application in tumor treatment, providing more precise and effective treatment means. In this work, we constructed temperature- and acid-responsive PP-TPZ-AFe-Y6 nanocapsules and evaluated their antitumor effects both in vitro and in vivo. The size of PP-TPZ-AFe-Y6 nanocapsules is around 200 nm, whose size can effectively utilize the EPR effect to target and deliver drugs to tumors more effectively. The nanocapsules feature excellent drug release control ability, which effectively promotes the release of internal chemotherapeutic drug TPZ and ferroptosis agent AFe under external stimulation. The released AFe participates in the Fenton reaction, converting H_2O_2 into toxic ·OH and inducing tumor cell death. The results of in vivo and in vitro experiments proved that the nanocapsules have promising biosafety and tumor therapeutic ability. This nanocapsules-based drug delivery system provides a practical approach for designing more efficient therapeutic solutions, presenting new hope for tumor treatment.

Funding

This work was financially supported by the National Natural Science Foundation of China (Nos. 22377026, 52001008), the National Key R&D Program of China (No. 2023YFB3507003), and the Guangzhou Basic and Applied Basic Research Foundation (No. 202201010669).

Conflicts of interest

The authors declare that they have no conflicts of interest.

Data availability statement

The data that support the findings of this study are available from the corresponding author upon reasonable request.

References

[1] Bai X, Ni J, Beretov J, et al. Cancer stem cell in breast cancer therapeutic resistance. *Cancer Treat Rev*. 2018;69:152–163.
[2] Riis M. Modern surgical treatment of breast cancer. *Ann Med Surg (Lond)*. 2020;56:95–107.
[3] Adesoye T, Lucci A. Current surgical management of inflammatory breast cancer. *Ann Surg Oncol*. 2021;28:5461–5467.
[4] Huang H, Zhou J, Chen H, et al. The immunomodulatory effects of endocrine therapy in breast cancer *J Exp Clin Cancer Res*. 2021;40(1):19.
[5] Zeng E, He W, Sjölander A, et al. Determinants and effectiveness of extending the duration of adjuvant hormone therapy beyond 5 years in patients with breast cancer. *Cancer Res*. 2022;82(19):3614–3621.
[6] Haque Md M, Desai KV. Pathways to endocrine therapy resistance in breast cancer. *Front Endocrinol*. 2019;10:573.
[7] Hartkopf AD, Grischke EM, Brucker SY. Endocrine-resistant breast cancer: mechanisms and treatment. *Breast Care (Basel)*. 2020;15(4):347–354.
[8] Stockwell BR. Ferroptosis turns 10: emerging mechanisms, physiological functions, and therapeutic applications. *Cell*. 2022;185(14):2401–2421.
[9] Dixon SJ, Lemberg KM, Lamprecht MR, et al. Ferroptosis: an iron-dependent form of nonapoptotic cell death. *Cell*. 2012;149(5):1060–1072.
[10] Stockwell BR, Friedmann Angeli JP, Bayir H, et al. Ferroptosis: a regulated cell death nexus linking metabolism, redox biology, and disease. *Cell*. 2017;171(2):273–285.
[11] He YJ, Liu XY, Xing L, et al. Fenton reaction-independent ferroptosis therapy via glutathione and iron redox couple sequentially triggered lipid peroxide generator. *Biomaterials*. 2020;241:119911.
[12] Zhou Q, Meng Y, Li D, et al. Ferroptosis in cancer: from molecular mechanisms to therapeutic strategies. *Signal Transduct Target Ther*. 2024;9(1):55.
[13] Blanco E, Shen H, Ferrari M. Principles of nanoparticle design for overcoming biological barriers to drug delivery. *Nat Biotechnol*. 2015;33(9):941–951.
[14] Sun Q, Sun X, Ma X, et al. Integration of nanoassembly functions for an effective delivery cascade for cancer drugs. *Adv Mater*. 2014;26(45):7615–7621.
[15] Ji J, Ma F, Zhang H, et al. Light-activatable assembled nanoparticles to improve tumor penetration and eradicate metastasis in triple negative breast cancer. *Adv Funct Mater*. 2018;28(33):1801738.
[16] Wang J, Fang Z, Zhao C, et al. Intelligent size-switchable iron carbide-based nanocapsules with cascade delivery capacity for hyperthermia-enhanced deep tumor ferroptosis. *Adv Mater*. 2024;36(9):2307006.
[17] Zeng Z, Peng Z, Chen L, et al. Facile fabrication of thermally responsive Pluronic F127-based nanocapsules for controlled release of doxorubicin hydrochloride. *Colloid Polym Sci*. 2014;292(7):1521–1530.

[18] Ke CJ, Chiang WL, Liao ZX, et al. Real-time visualization of pH-responsive PLGA hollow particles containing a gas-generating agent targeted for acidic organelles for overcoming multi-drug resistance. *Biomaterials*. 2013;34(1):1–10.
[19] Hu H, Ruan H, Ruan S, et al. Acid-responsive PEGylated branching PLGA nanoparticles integrated into dissolving microneedles enhance local treatment of arthritis. *Chem Eng J*. 2022;431:134196.
[20] Chen Y, Li X. Near-infrared fluorescent nanocapsules with reversible response to thermal/pH modulation for optical imaging. *Biomacromolecules*. 2011;12(12):4367–4372.
[21] Xing L, Liu XY, Zhou TJ, et al. Photothermal nanozyme-ignited Fenton reaction-independent ferroptosis for breast cancer therapy. *J Control Release*. 2021;339:14–26.
[22] Zhu G, Chi H, Liu M, et al. Multifunctional "ball-rod" Janus nanoparticles boosting Fenton reaction for ferroptosis therapy of non-small cell lung cancer. *J Colloid Interface Sci*. 2022;621:12–23.
[23] Chi H, Zhu G, Yin Y, et al. Dual-responsive multifunctional "core–shell" magnetic nanoparticles promoting Fenton reaction for tumor ferroptosis therapy. *Int J Pharm*. 2022;622:121898.
[24] Huang L, Feng J, Zhu J, et al. A strategy of Fenton reaction cycloacceleration for high-performance ferroptosis therapy initiated by tumor microenvironment remodeling. *Adv Healthcare Mater*. 2023;12(18):2203362.
[25] Henning Y, Blind US, Larafa S, et al. Hypoxia aggravates ferroptosis in RPE cells by promoting the Fenton reaction. *Cell Death Dis*. 2022;13(7):662.
[26] Yang WS, Stockwell BR. Synthetic lethal screening identifies compounds activating iron-dependent, nonapoptotic cell death in oncogenic-RAS-harboring cancer cells. *Chem Biol*. 2008;15(3):234–245.
[27] Yagoda N, Von Rechenberg M, Zaganjor E, et al. RAS–RAF–MEK-dependent oxidative cell death involving voltage-dependent anion channels. *Nature*. 2007;447(7146):865–869.
[28] Endale HT, Tesfaye W, Mengstie TA. ROS induced lipid peroxidation and their role in ferroptosis. *Front Cell Dev Biol*. 2023;11:1226044.
[29] Zhang Z, Yang J, Zhou Q, et al. The cGAS–STING-mediated ROS and ferroptosis are involved in manganese neurotoxicity. *J Environ Sci*. 2025;152:71–86.
[30] Wen Y, Li K, Ni M, et al. Dendritic polylysine with paclitaxel and triptolide codelivery for enhanced cancer ferroptosis through the accumulation of ROS. *ACS Appl Mater Interfaces*. 2024;16(16):20143–20156.
[31] Gu D, Liu M, Wu H, et al. Reactive oxygen-primed and autophagy inhibition-sensitized ferroptosis combined with photothermal ablation for tumor therapy. *ACS Mater Lett*. 2023;5(8):2243–2255.
[32] Zhu J, Wang X, Su Y, et al. Multifunctional nanolocks with GSH as the key for synergistic ferroptosis and anti-chemotherapeutic resistance. *Biomaterials*. 2022;288:121704.
[33] Chen M, Tong X, Sun Y, et al. A ferroptosis amplifier based on triple-enhanced lipid peroxides accumulation strategy for effective pancreatic cancer therapy. *Biomaterials*. 2024;309:122574.
[34] Li W, Liu S, Ding H, et al. Three-step depletion strategy of glutathione: tunable metal–organic-framework-engineered nanozymes for driving oxidative/nitrative stress to maximize ferroptosis therapy. *Nano Lett*. 2024;24(6):2071–2080.
[35] Wang W, Green M, Choi JE, et al. CD8+ T cells regulate tumour ferroptosis during cancer immunotherapy. *Nature*. 2019;569(7755):270–274.

How to cite this article: You J, Liu S, Liang J, Feng Q, Duan M, Ali Z, Chen L, Wang Z. Adaptive dual-responsive nanocapsules for precision ferroptosis-driven and chemotherapy-enhanced tumor ablation. MedMat 2024;1(2):e00008. doi: 10.1097/mm9.0000000000000008